

Non-thermal emission in lobes of radio galaxies: III. 3C 98, Pictor A, DA 240, Cygnus A, 3C 326, and 3C 236

Massimo Persic^{1,2,3}, Yoel Rephaeli^{4,5}

¹*INAF-Trieste Astronomical Observatory, via G.B. Tiepolo 11, I-34100 Trieste, Italy*

²*INFN-Trieste, via A. Valerio 2, I-34127 Trieste, Italy*

³*Physics & Astronomy Dept., Bologna University, via P. Gobetti 93/2, I-40129 Bologna, Italy*

⁴*School of Physics & Astronomy, Tel Aviv University, Tel Aviv 69978, Israel*

⁵*Center for Astrophysics and Space Sciences, University of California at San Diego, La Jolla, CA 92093, USA*

Accepted ... ; Received ... ; in original form ...

ABSTRACT

Recent analyses of the broad spectral energy distributions (SED) of extensive lobes of local radio-galaxies have confirmed the leptonic origin of their *Fermi*/LAT γ -ray emission, significantly constraining the level of hadronic contribution. SED of distant ($D_L > 125$ Mpc) radio-galaxy lobes are currently limited to the radio and X-ray bands, hence give no information on the presence of non-thermal (NT) protons but are adequate to describe the properties of NT electrons. Modeling lobe radio and X-ray emission in 3C 98, Pictor A, DA 240, Cygnus A, 3C 326, and 3C 236, we fully determine the properties of intra-lobe NT electrons and estimate the level of the related γ -ray emission from Compton scattering of the electrons off the superposed Cosmic Microwave Background, Extragalactic Background Light, and source-specific radiation fields.

Key words: galaxies: cosmic rays – galaxies: active – galaxies: individual: 3C 98 – galaxies: individual: 3C 236 – galaxies: individual: 3C 326 – galaxies: individual: DA 240 – galaxies: individual: Cygnus A – galaxies: individual: Pictor A – gamma rays: galaxies – radiation mechanisms: non-thermal

1 INTRODUCTION

Measurements of non-thermal (NT) emission from the extended lobes of radio galaxies provide a tangible basis for modeling of the spectral distributions of energetic particles in these environments. Sampling the spectral energy distributions (SED), even with only limited spatial information, yields valuable insight on the emitting electrons and possibly also on energetic protons whose p - p interactions in the ambient lobe plasma and ensuing π^0 -decay could yield detectable $\gtrsim 0.1$ GeV emission. In addition to the intrinsic interest in physical conditions in radio lobes, modeling energetic particles and their emission processes in these environments can yield clues to the origin of NT particles in galaxy clusters.

Currently available spectral radio, X-ray, and γ -ray measurements of the lobes of four radio galaxies have provided an adequate basis for determining the emission processes, the SED of the NT emitting particles, and the mean value of the magnetic field when the superposed photon fields in the lobe region are properly accounted for (Fornax A: Persic & Rephaeli 2019a, hereafter Paper I; Centaurus A, Centau-

rus B, and NGC 6251: Persic & Rephaeli 2019b, hereafter Paper II). These SED analyses have confirmed the leptonic origin of the measured lobe *Fermi*/LAT γ -ray emission, constraining the level of hadronic contribution to within several percent.

In the present paper we extend our SED analysis of radio-galaxy lobes to six relatively distant ($D_L > 125$ Mpc) sources with no available >0.1 GeV *Fermi*/LAT fluxes: 3C 98, Pictor A, DA 240, Cygnus A, 3C 326, and 3C 236. Lacking γ -ray data, the available spectral measurements enable determination of the electron spectral distribution, but can not directly constrain NT proton yields. Since the results presented here are based essentially on an identical treatment to that in Papers I and II, our discussion will be limited only to the most relevant observational data and to the results of our spectral modeling. In Section 2 we summarize the observational data and estimates of the radiation field densities in the lobes of the six galaxies. Results of the fitted SED models are detailed in Section 3 and discussed in Section 4. Our main conclusions are summarized in Section 5.

2 EMISSION AND RADIATION FIELDS IN THE LOBES

The six radio galaxies included in this analysis have elliptical hosts and a double-lobe morphology, with (usually) a flat radio lobe surface brightness. In this section we briefly discuss the sources, observations of NT emission, the lobe superposed radiation fields.

2.1 Observations of NT emission

3C 98 ($z = 0.0306$; luminosity distance $D_L = 126$ Mpc) shows a double-lobe morphology with a flat surface brightness distribution and a total angular extent of $5' \times 2'$ (Leahy et al. 1997). Broad-band total flux densities from a variety of radio telescopes, compiled in the NASA Extragalactic Database (NED), are listed in Table 1. NT X-ray emission, detected from each lobe, is interpreted as arising from Compton scattering of Cosmic Microwave Background (CMB) photons off radio emitting electrons (Isobe et al. 2005: *XMM-Newton* data). We assume a lobe radius $r = 30$ kpc and a galaxy to nearest lobe boundary distance $d = 26.5$ (see Isobe et al. 2005).

Pictor A ($z = 0.0342$; $D_L = 149$ Mpc) shows two symmetrical dim radio lobes with a bright compact hot spot on the far edge of the W lobe (connected with the radio nucleus by a faint jet) and two fainter, less compact spots on the E lobe (Perley et al. 1997). NT X-ray emission from the lobes, detected by Grandi et al. (2003, *XMM-Newton* data) and confirmed in its spatial extension by Hardcastle & Croston (2005, *Chandra* data; see also Hardcastle et al. 2016) and Migliori et al. (2007, *XMM-Newton* data), is interpreted as Compton/CMB radiation. The detected 0.2–200 GeV γ -ray emission is attributed to the jet (Brown & Adams 2012; *Fermi*/LAT data), based on its variability timescale ($\lesssim 1$ yr) and its incompatibility with the (well resolved) radio and X-ray emission within a synchrotron self-Compton SED model of a prominent compact hotspot in the Western lobe. Lobe NT SED data are reported in Table 2. We assume $r = 65$ kpc and $d = 15$ kpc (Perley et al. 1997).

DA 240 ($z = 0.03566$; $D_L = 152$ Mpc; $\theta \sim 35'$), 3C 326 ($z = 0.0895$; $D_L = 395$ Mpc; $\theta \sim 20'$), and 3C 236 ($z = 0.1005$; $D_L = 449$ Mpc; angular extent $\theta \sim 40'$) have 0.326–10.6 GHz data from the entire sources and from their individual components (Mack et al. 1997). NT X-ray emission, detected from the E lobe of DA 240 and the W lobes of 3C 326 and 3C 236, is interpreted as Compton/CMB radiation (3C 236: Isobe & Koyama 2015; 3C 326: Isobe et al. 2009; DA 240: Isobe et al. 2011 – *Suzaku* data). Lobe SED data for the three sources are reported in Tables 3–5. We assume $r = 400$ kpc and $d = 850$ kpc for 3C 236 (Isobe & Koyama 2014), $r = 225$ kpc and $d = 515$ kpc for 3C 326 (see Ogle et al. 2007 and Isobe et al. 2009), and $r = 268.5$ kpc and $d = 190$ kpc for DA 240 (Isobe et al. 2011).

Cygnus A ($z = 0.0561$; $D_L = 237$ Mpc), with multi-frequency radio (VLA) and X-ray (*Chandra*) emissions available for both lobes separately (Yaji et al. 2010; de Vries et al.

2018), is the brightest radio galaxy in the sky (Birzan et al. 2004). NT X-ray emission from both lobes is interpreted as Compton scattering off the CMB and from synchrotron radiation from the lobes (Yaji et al. 2010; de Vries et al. 2018). Within the relative paucity of data, the lobe SEDs appear to be different, with that of the E-lobe steeper/flatter than that of the W-lobe at radio/X-ray frequencies (Yaji et al. 2010; de Vries et al. 2018). Lobe NT SED data are reported in Table 6. We assume $r = 16.3$ kpc and $d = 61.3$ kpc (Yaji et al. 2010).

2.2 Radiation fields

A precise determination of the ambient photon fields in the lobes is needed to predict X/ γ -ray emission from Compton scattering of radio-emitting electrons. Radiation fields in the lobes include cosmic and local components.

Cosmic radiation fields include the CMB and the Extragalactic Background Light (EBL). The CMB is a pure Planckian with $T_{\text{CMB}} = 2.725$ K and energy density $u_{\text{CMB}} = 0.25(1+z)^4 \text{ eV cm}^{-3}$ (e.g., Dermer & Menon 2009). The EBL, originating from direct and dust-reprocessed starlight integrated over the star formation history of the universe (e.g., Franceschini & Rodighiero 2017; Acciari et al. 2019), can be represented as a suitable combination of diluted Planckians (see Paper II).

Local radiation fields (Galaxy Foreground Light, GFL) arise from the elliptical host galaxies, whose SEDs usually show two thermal humps, IR and optical.

(i) 3C 98's host galaxy has a bolometric IR luminosity $L_{\text{IR}} < 4.1 \cdot 10^{43} \text{ erg s}^{-1}$, as implied by *IRAS* flux densities at 12, 25, 60 and $100 \mu\text{m}$ (Golombek et al. 1988)¹. The optical bolometric luminosity $L_{\text{opt}} \sim 2.3 \cdot 10^{44} \text{ erg s}^{-1}$ is derived from $V = 14.12$ mag (Smith & Heckman 1989a) applying the bolometric correction ($BC_V = -0.85$, Buzzoni et al. 2006), so that $m_{\text{opt}}^{\text{bol}} = V + BC_V$ (see Paper I).

(ii) Pictor A's host has $L_{\text{IR}} \sim 1.3 \cdot 10^{44} \text{ erg s}^{-1}$, estimated from the f_{12} , f_{25} , f_{60} (Singh et al. 1990) and f_{100} (inferred from f_{60} , see Lisenfeld et al. 2007) *IRAS* flux densities; and $L_{\text{opt}} \sim 1.2 \cdot 10^{44} \text{ erg s}^{-1}$, estimated from $B = 15.95$, $(B-V) = 0.73$ (from NED) applying the bolometric correction.

(iii) DA 240's host has $L_{\text{opt}} \sim 5 \cdot 10^{45} \text{ erg s}^{-1}$, estimated from $R = 10.7$ mag (Peng et al. 2004) converted to V mag using $(B-V) = 0.90$ ² and applying the bolometric correction. $L_{\text{IR}} \sim 6 \cdot 10^{45} \text{ erg s}^{-1}$ is estimated from L_B through Bregman et al.'s (1998) FIR-B relation assuming $L_{\text{IR}} \sim 2 L_{\text{FIR}}$ (Persic & Rephaeli 2007).

(iv) Cygnus A's host has $L_{\text{IR}} \sim 1.9 \cdot 10^{45} \text{ erg s}^{-1}$ (Golombek et al. 1988), and $L_{\text{opt}} \sim 1.5 \cdot 10^{45} \text{ erg s}^{-1}$ estimated from

¹ The total IR (8–1000 mm) flux is $f_{\text{IR}} = 1.8 \cdot 10^{-11} (13.48 f_{12} + 5.16 f_{25} + 2.58 f_{60} + f_{100}) \text{ erg cm}^{-2} \text{ s}^{-1}$ (Sanders & Mirabel 1996), where f_{12} , f_{25} , f_{60} , f_{100} are the *IRAS* flux densities at the indicated wavelengths (in μm).

² www.aerith.net/astro/color_conversion.html

Table 1. Emission from the lobes of 3C 98.

Frequency Log(ν /Hz)	Flux Density [Jy]	Frequency Log(ν /Hz)	Flux Density [Jy]	Frequency Log(ν /Hz)	Flux Density [Jy]	Frequency Log(ν /Hz)	Flux Density [Jy]
7.167	480 \pm 110	7.934	94.3 \pm 2.2	8.875	16.7 \pm 0.3	9.699	3.29
7.223	420 \pm 80	8.204	49.1 \pm 6.4	8.875	16.0 \pm 0.8	9.699	4.97 \pm 0.25
7.301	390 \pm 66	8.250	44.0 \pm –	9.146	10.2 \pm 0.5	9.699	4.94 \pm 0.25
7.301	289 \pm 29	8.250	48.8 \pm 3.9	9.146	10.3 \pm 0.3	9.700	4.73 \pm 0.31
7.347	312 \pm 43.3	8.250	51.4 \pm 2.6	9.146	9.75 \pm 0.2	9.700	3.39 \pm 0.12
7.348	312 \pm 30	8.250	35.5 \pm 2.8	9.146	9.9 \pm 0.5	9.903	3.08 \pm 0.07
7.398	260 \pm 52	8.250	50.6 \pm 2.5	9.146	11.1	10.029	2.82 \pm 0.12
7.398	285 \pm 34	8.250	47.2 \pm 4.7	9.149	12.0 \pm 0.3	10.029	3.01 \pm 0.13
7.420	215 \pm 18	8.502	29.7 \pm 1.1	9.423	7.30 \pm 0.20	10.362	1.35 \pm 0.20
7.420	218 \pm 17	8.611	26.9	9.431	7.01 \pm 0.35	10.362	1.20 \pm 0.12
7.580	147 \pm 22	8.611	21.3 \pm 0.9	9.431	7.09 \pm 0.10	10.519	1.10 \pm 0.10
7.580	160 \pm 7.2	8.611	24.2 \pm 4.6	9.431	7.17 \pm 0.35	10.613	0.7 \pm 0.2
7.580	173 \pm 8.7	8.611	27.5	9.431	6.10	10.795	0.3 \pm 0.3
7.778	132 \pm 30	8.670	26.7 \pm 1.5	9.679	2.70	10.973	0.1 \pm 0.5
7.869	98 \pm 1.1	8.803	20.9 \pm 0.4	9.686	3.13 \pm 0.43	17.383	(15.6 \pm 2.5) E–9
7.903	90 \pm 13	8.875	16.7 \pm 0.8	9.686	5.05 \pm 0.76		
7.903	83 \pm –	8.875	17.7 \pm 0.3	9.699	4.93 \pm 0.12		

Data: NED (radio), Isobe et al. (2005; X-rays). Unspecified flux errors are assumed to be at the 10% level.

Table 2. Emission from the lobes of Pictor A.

Frequency Log(ν /Hz)	East Lobe [Jy]	West Lobe [Jy]
7.869	237	213
8.515	86.3	94.3
9.166	27.4	32.9
9.699	8.77	12.0
17.383	(55 \pm 2) E–9	(55 \pm 2) E–9

Data: Perley et al. (1997; radio), Hardcastle & Croston (2005; X-rays – see also Hardcastle et al. 2016). Errors on radio fluxes are assumed to be at the 10% level.

Table 3. Emission from the W lobe of DA 240.

Frequency Log(ν /Hz)	Flux Density [mJy]	Frequency Log(ν /Hz)	Flux Density [mJy]
8.513	10299.0 \pm 120.4	9.677	1186.6 \pm 23.4
8.785	5688.7 \pm 78.1	10.023	749.3 \pm 27.8
9.431	1809.6 \pm 31.2	17.383	(51.5 \pm 7.0) E–6

Data: Mack et al. (1997; radio), Isobe et al. (2011; X-rays).

$V = 13.46$ (total, extinction corrected; Smith & Heckman 1989b) applying the bolometric correction. The IR emission is (Privon et al. 2012) mostly ($\sim 90\%$) torus-reprocessed radiation by an optically obscured ($A_V > 50$ mag, Imanishi & Ueno 2000) AGN (Antonucci et al. 1994; Carilli et al. 2019) with additional contributions from a dust-enshrouded starburst ($\gtrsim 6\%$) and a synchrotron jet ($\lesssim 4\%$).

(v) 3C 326’s host has $L_{\text{IR}} \sim 1.3 \cdot 10^{43}$ erg s $^{-1}$ (Ogle et al. 2007), and $L_{\text{opt}} \sim 1.2 \cdot 10^{44}$ erg s $^{-1}$ derived from L_B which is deduced from $L_{\text{FIR}} \sim 1/2 L_{\text{IR}}$ (e.g. Persic & Rephaeli 2007) through a FIR-B relation (Bregman et al. 1998).

Table 4. Emission from the lobes of Cygnus A.

Frequency Log(ν /Hz)	East Lobe [Jy]	West Lobe [Jy]
9.129	594 \pm 36	429 \pm 29
9.231	463 \pm 29	357 \pm 24
9.656	129 \pm 10	122 \pm 9
9.699	115 \pm 9	108 \pm 9
17.383	(71 \pm 10) E–9	(50 \pm 13) E–9

Data: Yaji et al. (2010; radio), de Vries et al. (2018; X-rays).

Table 5. Emission from the W lobe of 3C 326.

Frequency Log(ν /Hz)	Flux Density [mJy]	Frequency Log(ν /Hz)	Flux Density [mJy]
8.513	1534.6 \pm 22.9	9.677	232.1 \pm 2.4
8.785	982.5 \pm 18.8	10.023	114.1 \pm 5.6
9.431	933.6 \pm 43.7	17.383	(19.4 \pm 4.4) E–6

Data: Mack et al. (1977; radio), Isobe et al. (2009; X-rays).

Table 6. Emission from the W lobe of 3C 236.

Frequency Log(ν /Hz)	Flux Density [mJy]	Frequency Log(ν /Hz)	Flux Density [mJy]
8.513	588.1 \pm 22.3	9.677	36.4 \pm 14.4
8.785	348.6 \pm 18.3	10.023	40.3 \pm 16.3
9.431	153.0 \pm 18.3	17.383	(12.3 \pm 2.8) E–6

Data: Mack et al. (1997; radio), Isobe & Koyama (2014; X-rays).

(vi) 3C 236's central galaxy has $L_{\text{IR}} < 4.1 \cdot 10^{43} \text{ erg s}^{-1}$ (see Golombek et al. 1988), and $L_{\text{opt}} \sim 6.9 \cdot 10^{44} \text{ erg s}^{-1}$ derived from $V = 15.72 \text{ mag}$ (Smith & Heckman 1989b) applying the bolometric correction.

These IR and optical parameters allow us to model the GFL; in our calculations we take $T_{\text{gal, OPT}} = 2900 \text{ K}$ and $T_{\text{gal, IR}} = 29 \text{ K}$ (see PR19). The lobe X-ray data are spatial averages, so we correspondingly compute volume-averaged Compton/GFL yields, based on the fact that lobe radii and projected distances (from central galaxies) are much larger than the corresponding central-galaxy radii³, we treat galaxies as point sources (see Paper II).

3 MODELLING LOBE NT EMISSION

Radio emission in the lobes is by electron synchrotron in a disordered magnetic field whose mean value B is taken to be spatially uniform, and X- γ emission is by electron Compton scattering off the CMB and optical radiation fields. The calculations of the emissivities from these processes are standard (see Paper I). Assuming steady state, the electron energy distribution (EED) is assumed to be a time independent, spatially isotropic, truncated-PL distribution in the electron Lorentz factor, $N_e(\gamma) = N_{e0} \gamma^{-q_e}$ in the interval $[\gamma_{\text{min}}, \gamma_{\text{max}}]$, with a finite γ_{max} .

In all cases but Cyg A, the photoelectrically absorbed⁴ 1 keV flux density is used to determine N_{e0} assuming the emission is Compton/CMB. Cyg A is a notable exception because, due to its much higher magnetic field (than the other sources studied here, and in Papers I and II), as revealed by its very high radio to X-ray emission ratio, the synchrotron energy density in its lobes ($u_s = 0.55 \text{ eV cm}^{-3}$, in the range $10^5\text{-}10^{11} \text{ Hz}$) exceeds the CMB energy density, such that synchrotron-self-Compton (SSC) radiation contributes to the 1 keV flux even more than that of Compton/CMB. In calculating the SSC yield (see Eq. 11 in Paper I) we used an analytical expression for the synchrotron photon density field (deduced from a fit to the radio synchrotron spectrum⁵), $n_s(\epsilon) = N_{s,0} (\epsilon/\epsilon_0)^{-(\alpha+1)} e^{-\epsilon/\epsilon_0} \text{ cm}^{-3} \text{ erg}^{-1}$, with $N_{s,0} = (r_s/c) A_s$ and ϵ_0 the photon energy corresponding to 7 GHz (combined lobes), 6 GHz (E lobe), and 9 GHz (W lobe) and $\alpha = (q_e - 1)/2 = 0.75$. Given $n_s(\epsilon)$ and $n_{\text{CMB}}(\epsilon)$, we determined N_{e0} for Cyg A by fitting the combination of predicted SSC and Compton/CMB emissions to the measured 1 keV flux.

³ Effective radii estimated from B-luminosities (Romanishin 1986), or isophotal radii (Smith & Heckman 1989a).

⁴ 3C 98: $N_H = 1.17 \cdot 10^{21} \text{ cm}^2$ (Isobe et al. 2005); 3C 236: $N_H = 0.93 \cdot 10^{20} \text{ cm}^2$ (Hardcastle et al. 2016); 3C 326: $N_H = 3.84 \cdot 10^{20} \text{ cm}^2$ (Dickey & Lockman 1990); DA 240: $N_H = 0.49 \cdot 10^{21} \text{ cm}^2$ (Isobe et al. 2011); Cygnus A: $N_H = 0.31 \cdot 10^{22} \text{ cm}^2$ (De Vries et al. 2018); Pictor A: $N_H = 0.42 \cdot 10^{21} \text{ cm}^2$ (Hardcastle & Croston 2005).

⁵ The synchrotron emissivity we used to fit the radio flux spectrum is analytically given by $\eta(\nu) = A_s (\nu/\nu_*)^{-\alpha} e^{-(\nu/\nu_*)} \text{ erg s}^{-1} \text{ cm}^{-3} \text{ Hz}^{-1}$, with (for total lobe emission) $A_s = 10^{-34.65}$ and $\nu_* = 7 \text{ GHz}$.

Matching the synchrotron prediction to the radio spectrum yields q_e (from its featureless PL portion) and γ_{max} from the (hint of) spectral turnover at high energies. The minimum electron energy, γ_{min} , can be estimated directly from the 1 keV Compton/CMB data: $\gamma_{\text{min}} = 100$, corresponds to the transition between Coulomb and synchrotron-Compton losses (Paper II). With the electron spectrum fully specified, normalization of the predicted synchrotron spectral flux to the radio measurements yields B . The model SED and data are shown in Fig. 1.

As is apparent from Fig. 1, the radiative (synchrotron and Compton) yields of energetic electrons in the lobe SEDs analyzed here account for the currently available radio and X-ray data. This basic result of our spectral analyses strengthens a similar conclusion reached in earlier analyses (see Section 2.1).

4 DISCUSSION

The main conclusions of our analysis of the lobe SEDs of 3C 98, 3C 236, 3C 326, DA 240, Cygnus A, and Pictor A are quite similar to those presented in earlier papers where the original data for these sources were reported (see Section 2.1). However our treatment, first presented in Paper I, differs appreciably from those in previous analyses. We provide model SEDs for all sources using one simple EED (i.e., a single truncated PL) – whereas previous studies did not explicitly model the SED (3C 98, Isobe et al. 2005; 3C 236, Isobe & Koyama 2015; 3C 326, Isobe et al. 2009; DA 240, Isobe et al. 2011), or did so using a broken PL (Cygnus A, Yaji et al. 2010 and deVries et al. 2018; Pictor A, Hardcastle & Croston 2005). Our essentially uniform treatment allows us to compare the radiative properties of different lobes more directly and in a less constrained way.

The electron energy density is determined by integration over their spectral distribution with PL index $q_e - 1$ at energies below the characteristic value at which Coulomb losses are roughly equal to radiative losses, $\gamma < \gamma_{\text{min}}$, and with index q_e for $\gamma > \gamma_{\text{min}}$ (e.g., Rephaeli & Persic 2015). In Table 7 we list estimated values of the electron and magnetic energy densities for the lobes under study. The electron to magnetic energy density ratios are in the range $\mathcal{O}(10\text{-}100)$, suggesting a particle-dominated NT energy budget in the lobes. As mentioned, we cannot directly constrain proton contents in these lobes (unlike the case of Centaurus A, see Paper II), however the energy density of NT protons is probably much higher than that of NT electrons (see Paper II and Persic & Rephaeli 2014). If so, this further substantiates the validity of the result that most of the lobe NT energy density is in energetic electrons and protons.

Our analysis indicates that a GFL contribution to the predicted Compton yields in the *Fermi*/LAT band⁶ is negligible in 3C 236 and 3C 326, dominant in Cyg A, and compa-

⁶ We use projected galaxy-to-lobe distances (inclinations are unknown), so inferred GFL densities are strict upper limits.

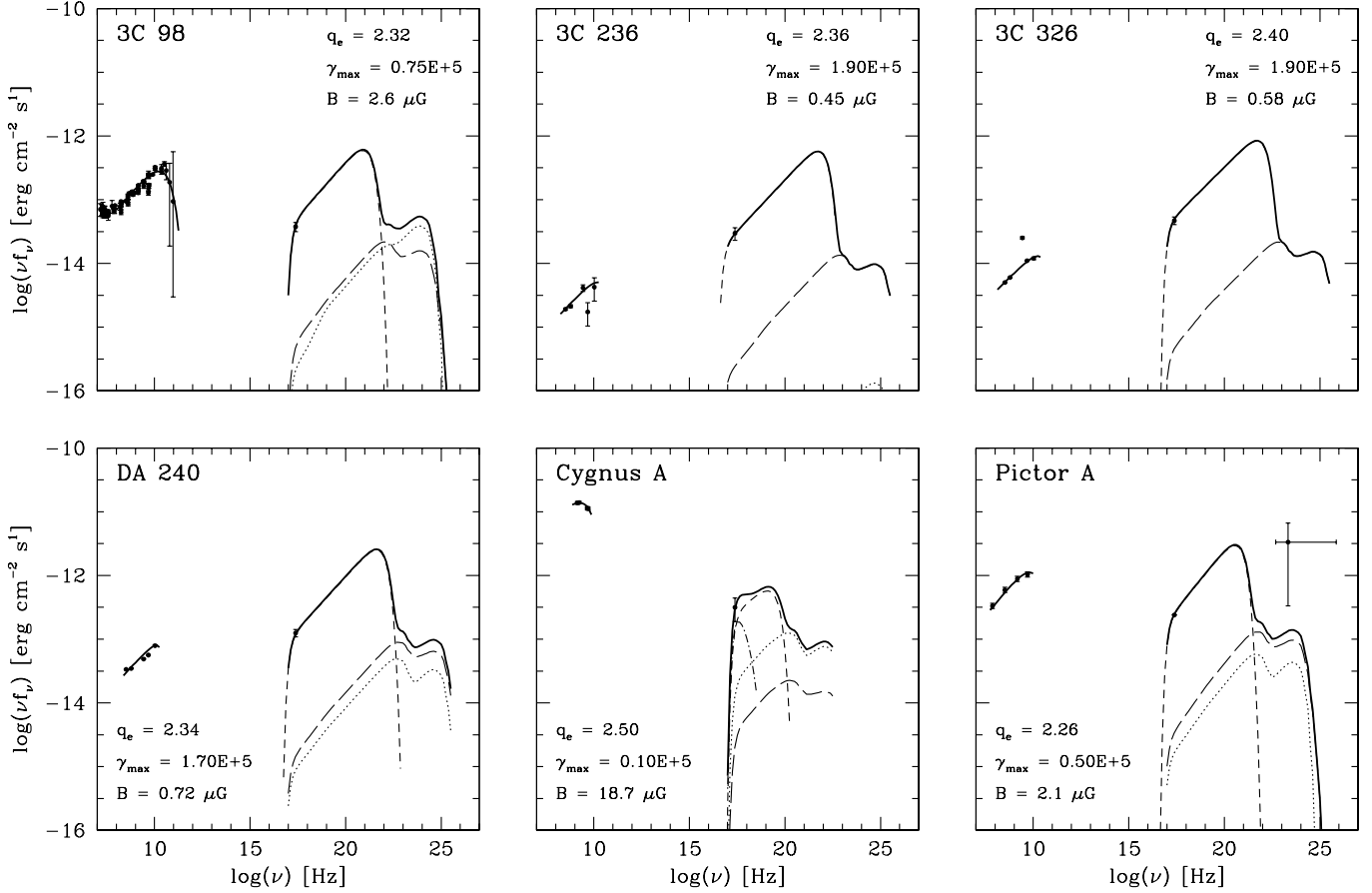


Figure 1. Data are denoted by dots (with error bars). Emission component curves are: synchrotron, solid; Compton/CMB, short-dashed; SSC, dot-dashed (Cyg A); Compton/EBL, long-dashed; Compton/GFL, dotted; total Compton: thick solid. Indicated in each panel are the values of the EED parameters. For Cygnus A we show total lobe SED; the separate lobe SEDs are displayed in Fig. (2). In Pictor A's SED we also show the lowest detected γ -ray flux (Brown & Adams 2012). Upper limits to IR luminosities (see Section 2.2) are treated as nominal IR luminosities.

rable to the EBL contribution in 3C 98, DA 240, and Pic A. The case of Cyg A is similar to that of Fornax A; in the lobes of both systems the dominant radiation field is the GFL, not the EBL. Note that γ -ray emission from the Fornax A lobes was measured by *Fermi*/LAT (see Paper I).

The lobes of Cyg A appear to have somewhat different SEDs, as was already noted (Yaji et al. 2010). In our simple truncated-PL characterization the difference is described by different EED high-energy cutoffs and magnetic fields. The radio spectrum shows a high-end spectral turnover at lower frequency in the E lobe than in the W lobe (Fig. 2). The shortest electron lifetime in the lobes, $\tau = 10^{11} \left(\frac{4}{3} \frac{\sigma_T}{m_e c} \gamma_{max} \frac{u_{mag} + u_{syn} + u_{CMB}}{u_{CMB}} \right)^{-1}$ s (for the assumed isotropic electron distribution), is 0.26 Myr in the E lobe ($u_{syn}^E = 0.75$ eV cm $^{-3}$) and 0.18 Myr in the W lobe ($u_{syn}^W = 0.37$ eV cm $^{-3}$). If the electron spectrum has attained a steady-state, possibly by *in situ* re-acceleration, then the different lifetimes would imply that the process is more efficient in the W lobe.

The γ -ray emission of Pic A observed by *Fermi*/LAT is unlikely to be related to the radio and X-ray emissions of a prominent compact hotspot in the Western lobe because a

synchrotron self-Compton SED model linking the emissions in all three bands proves impossible (Brown & Adams 2012). Indeed, the possibility that this γ -ray emission has a diffuse origin in the lobes can essentially be ruled out based on the following considerations: Lobe origin would require an EED normalization, N_{e0} , higher by an order of magnitude than in the no- γ -ray case. Such a high value of N_{e0} would require an unusually high low-energy cutoff, $\gamma_{min} = 2500$, to account for the 1 keV flux, and obviously a low magnetic field, $B = 0.37$ μ G, to fit the radio spectrum (see Fig. 3). The combination of high N_{e0} and low B would imply $u_e/u_B \sim 1.8 \cdot 10^4$, an unusually high value in radio lobes (see Table 7, and Table 1 of Paper II).

The predicted Compton/(EBL+GFL) γ -ray emission in the *Fermi*/LAT band is well below the LAT sensitivity, $\sim 10^{-12}$ erg s $^{-1}$ at 1 GeV (5σ detection for 10 yr sky-survey exposure at high Galactic latitude; Principe et al. 2018) in all cases considered here. The average γ -ray to radio flux ratio, ϕ , at their respective peaks (in νf_ν units) is $\phi \sim 1$ for 3C 236, 3C 326, and DA 240, $\phi \sim 0.1$ for 3C 98 and Pic A, and $\phi \sim 0.01$ for Cyg A; and it is $\phi \sim 1$ for Fornax A,

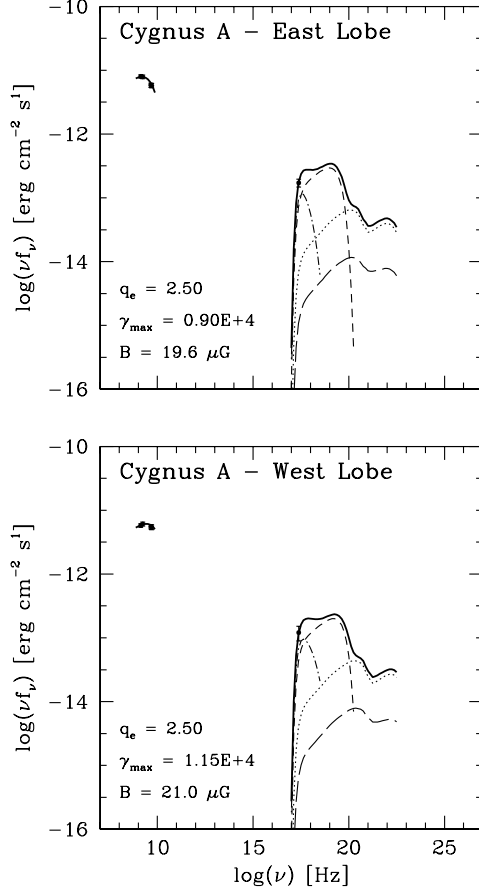


Figure 2. The SEDs of the E lobe (top) and the W lobe (bottom) of Cyg A. Symbols are as in Fig.(1).

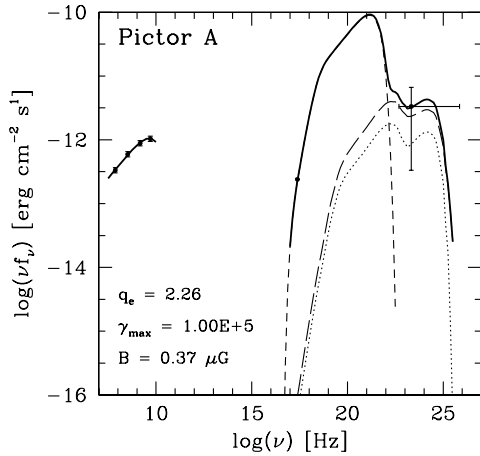


Figure 3. The SED of Pic A assuming the lowest γ -ray flux measured by *Fermi*/LAT (Brown & Adams 2012) is diffuse lobe emission. Symbols are as in Fig.(1).

Cen A, Cen B, and $\phi \sim 100$ for NGC 6251 (Paper II). Low ϕ -ratios are a consequence of low γ_{max} : for example Cyg A, with $\gamma_{max} = 10^4$ (lowest value in the set), has the lowest ϕ , whereas NGC 6251, with $\gamma_{max} = 1.1 \cdot 10^6$ (highest value in the sample), has the highest- ϕ ; and other sources (e.g., Fornax A, Cen A) with intermediate values ($\gamma_{max} \sim 10^5$) have

$\phi \sim 1$. If, hypothetically, the radio data for Cyg A required $\gamma_{max} \sim 10^5$, the predicted γ -ray flux would be $\gtrsim 10^{-12}$ erg s $^{-1}$ at 1 GeV, detectable with *Fermi*/LAT. Thus, it appears that, apart from the obvious geometrical dimming, the predicted very low γ -ray fluxes reflect intrinsic properties of the electron populations in the halos.

Cyg A is of particular interest with regard to the feasibility of γ -ray detection. Due to the low value of γ_{max} the Compton/(EBL+GFL) hump cuts off at $\log(\nu) \sim 22.5$, i.e. ~ 100 MeV, just short of the *Fermi*/LAT range. If so, we would expect any detectable emission above this energy to be of pionic origin. This situation, along with the relatively high value of the thermal gas density in the lobes (Yaji et al. 2010)⁷, make the lobes of Cyg A interesting sources of pion-decay γ rays. The issue, of course, is the level of such emission. Consider a proton energy distribution, $N(E_p) = N_{p0}(E_p/\text{GeV})^{-q_p}$ with $q_p = 2.2$ and $E_p^{max} = 50$ GeV. The former value is suggested by considerations of a moderately strong non-relativistic acceleration mechanism ($q_p = (R+2)/(R-1)$, with compression ratio $R \sim 3.5$), and of relatively low proton energy losses in the lobe environment (cf. the inelastic pp -interaction cross section in the relevant energy range, $\sigma_{pp} \sim 30$ mbarn; e.g. Kelner et al. 2006). The value of E_p^{max} is not crucial; lower (higher) values in the range ~ 5 -100 GeV just make the pion hump somewhat narrower (broader). The energy density of the relativistic electrons, 1440 eV cm^{-3} , corresponds to a relativistic electron pressure of $p_e = u_e/3 = 7.7 \cdot 10^{-10} \text{ dyn cm}^{-2}$. To this we add the thermal pressure in the lobes, $p_{th} = n_H k_B T = 0.7 \cdot 10^{-10} \text{ dyn cm}^{-2}$ (from $n_H \sim 1.4 \cdot 10^{-2} \text{ cm}^{-2}$ and $k_B T = 5.11 \text{ keV}$; Yaji et al. 2010). As magnetic pressure is negligible, the (spectrally derived) total pressure is $p = p_e + p_{th} = 8.4 \cdot 10^{-10} \text{ dyn cm}^{-2}$. The latter value may be compared with the pressure, $p = 8.6 \cdot 10^{-10} \text{ dyn cm}^{-2}$ (Snios et al. 2018), in the surrounding "X-ray cocoon" (a.k.a. "X-ray cavity": Wilson et al 2006) that envelopes Cyg A. Assuming the lobes to be in pressure equilibrium with the cocoon (e.g. Mathews & Guo 2010), we derive a NT proton pressure $p_p = 0.2 \cdot 10^{-10} \text{ dyn cm}^{-2}$: the corresponding energy density is $u_p = 3p_p = 30 \text{ eV cm}^{-3}$. Hence, $N_{p0} = 1.1 \cdot 10^{-8} \text{ cm}^{-3}$. The derived low proton content suggests that the relativistic fluid in the Cyg A lobes consists mainly of electron pairs, rather than a relativistic electron-proton plasma (e.g., Mathews 2014). This would indicate that energetic particles were transferred to the lobes by a "light" jet whose matter component consists largely of pair plasma (e.g., English et al. 2016; Snios et al. 2018). The resulting lepto-hadronic model is plotted in Fig. 4, which clearly demonstrates that,

⁷ The lack of internal depolarization in the lobes implies $n_H < 2 \cdot 10^{-4} \text{ cm}^{-3}$, assuming no field reversals in the lobes (Dreher et al. 1987). This results is clearly inconsistent, by 2 orders of magnitude, with the result of Yaji et al. (2010) who fit the X-ray spectra from the Cyg A lobes with a thermal + PL model. As suggested by Yaji et al., the discrepancy could be explained by a tangled field morphology.

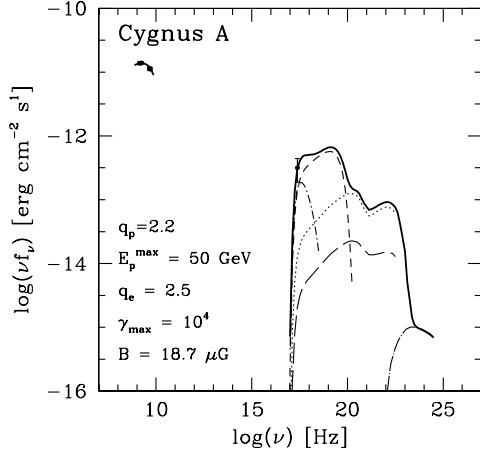


Figure 4. The lepto-hadronic model of the total lobe SED of Cyg A. Data are denoted by dots (with error bars). Emission component curves are: synchrotron, solid; Compton/CMB, short-dashed; SSC, dot-short-dashed; Compton/EBL, long-dashed; Compton/GFL, dotted; pionic, dotted-long-dashed; total Compton and pionic: thick solid. Indicated are the values of the proton and electron spectral parameters.

Table 7. Energy densities (eV cm^{-3}) in the lobes.

$u_{e,B}$	3C 98	3C 236	3C 326	DA 240	Cyg A	Pic A
u_e	19.5	0.04	0.38	0.11	1440	8.2
u_B	0.17	0.005	0.008	0.013	8.70	0.11
$\frac{u_e}{u_B}$	115	8	47.5	8.5	165.5	74.3

even if weak, π^0 -decay emission is likely to dominate emission in the *Fermi*/LAT band.

5 CONCLUSION

Spectral distributions of NT electrons in lobes of radio galaxies can be directly determined from radio and X-ray measurements. Only weak upper limits can be set on energetic protons when there are no γ -ray measurements of the lobes.

Modeling radio and X-ray measurements from several such lobes (3C 98, Pictor A, DA 240, Cygnus A, 3C 326, and 3C 236 – located at $D_L > 125$ Mpc) as having synchrotron and Compton origin, we fully determine the spectral properties of the emitting electrons.

The main conclusion of our present analysis is that when NT X-ray emission measured for these sources is interpreted as Compton/CMB (including SSC, in the case of Cyg A) radiation, the ensuing SED (leptonic) models are similar to those for sources whose observational SEDs extend to the *Fermi*/LAT γ -ray band (see Papers I and II).

We do confirm earlier suggestions on the Compton/CMB nature of the diffuse X-ray emission from the original data papers. However, our treatment differs from those in previous analyses: we model all SEDs using a truncated single-PL EED, whereas the earlier studies either did not explicitly model the SED or did so using a broken PL. Our uniform

treatment allows us to compare properties of different lobe SEDs in a more unbiased and direct way.

We predict the Compton/(EBL+GFL) emission in the lobes using a recent EBL model (Franceschini & Rodighiero 2017; Acciari et al. 2019) and by accounting for the host galaxy contribution (GFL) to the superposed radiation fields in the lobes. Very low Compton fluxes in the *Fermi*/LAT band are predicted from sources whose radio spectra imply EEDs with low γ_{max} .

For Cyg A we predict the Compton emission to be negligible at energies $\gtrsim 100$ MeV, so any detectable emission in this spectral band would be of pionic origin and may allow a direct determination of the NT proton content.

ACKNOWLEDGEMENTS

We used the NASA/IPAC Extragalactic Database (NED), which is operated by the Jet Propulsion Laboratory, Caltech, under contract with NASA. We acknowledge useful comments by an anonymous referee.

REFERENCES

- Acciari V., et al. (MAGIC Collab.), 2019, MNRAS, 486, 4233
 Antonucci R., Hurt T., Kinney A., 1994, Nature, 371, 313
 Birzan L., Rafferty D.A., McNamara B.R., Wise M.W., Nulsen P.E.J., 2004, ApJ, 607, 800
 Bregman J.N., Snider B.A., Grego L., Cox C.V., 1998, ApJ, 499, 670
 Brown A.M., Adams J., 2012, MNRAS, 421, 2303
 Buzzoni A., Arnaboldi M., Corradi R.L.M., 2006, MNRAS, 368, 877
 Carilli C.R., Perley R.A., Dhawan V., Perley D.A., 2019, ApJ, 874:L32
 Dermer C.D., Menon G., 2009, High Energy Radiation from Black Holes (Princeton, NJ: Princeton University press)
 De Vries M.N., Wise M.W., Huppenkothen D., et al., 2018, MNRAS, 478, 4010
 Dickey J.M., Lockman F.J., 1990, ARA&A, 28, 215
 Dreher J.W., Carilli C.L., Perley R.A., 1987, 316, 611
 English W., Hardcastle M.J., Krause M.G.H., 2016, MNRAS, 461, 2025
 Franceschini A., Rodighiero G., 2017, A&A, 603, A 34 (and Erratum: 2018, A&A, 614, C 1)
 Golombek D., Miley G.K., Neugebauer G., 1988, AJ, 95, 26
 Grandi P., Guainazzi M., Maraschi L., et al. 2003, ApJ, 586, 123
 Hardcastle M.J., Croston J.H., 2005, MNRAS, 363, 649
 Hardcastle M.J., Lenc E., Birkinshaw M., et al., 2016, 455, 3526
 Imanishi M., Ueno S., 2000, ApJ, 525, 626
 Isobe N., Koyama S., 2015, PASJ, 67, 77
 Isobe N., Makishima K., Tashiro M., Hong S. 2005, ApJ, 632, 781
 Isobe N., Seta H., Tashiro M.S. 2011, PASJ, 63, S947
 Isobe N., Tashiro M.S., Gandhi P., et al., 2009, ApJ, 706, 454
 Kelner S.R., Aharonian F.A., Bugayov V.V., 2006, Phys Rev D, 74(3), 034018
 Lisenfeld U., Verdes-Montenegro L., Sulentic J., et al. 2007, A&A, 462, 507
 Leahy J.P., Black A.R.S., Dennett-Thorpe J., et al., 1997, MNRAS, 291, 20
 Mack K.-H., Klein U., O’Dea C.P., Willis A.G., 1997, A&AS, 123, 423
 Mathews W.G., 2014, ApJ, 783:42

- Mathews W.G., Guo F., 2010, ApJ, 725, 1440
- Migliori G., Grandi P., Palumbo G.G.C., et al., 2007, ApJ, 668, 203
- Ogle P., Antonucci R., Appleton P.N., Whysong D., 2007, ApJ, 668, 699
- Peng B., Strom R.G., Wei J., Zhao Y.H., 2004, A&A, 415, 487
- Perley R.A., Röser H.-J., Meisenheimer K., 1997, A&A, 328, 12
- Persic M., Rephaeli Y., 2007, A&A, 463, 481
- Persic M., Rephaeli Y., 2014, A&A, 567, A 101
- Persic M., Rephaeli Y., 2019a, MNRAS, 485, 2001 (and Erratum: 2019, MNRAS, 486, 950) (Paper I)
- Persic M., Rephaeli Y., 2019b, MNRAS, 490, 1489 (Paper II)
- Principe G., Malyshev D., Ballet J., Funk S., 2018, A&A, 618, A22
- Privon G.C., Baum S.A., O’Dea C.P., et al., 2012, ApJ, 747:46
- Rephaeli Y., Persic M., 2015, ApJ, 805:111
- Romanishin W., 1986, AJ, 91, 76
- Sanders D.B., Mirabel I.F. 1996, ARAA, 34, 749
- Singh K.P., Rao A.R., Vahia M.N., 1990, MNRAS, 246, 706
- Smith E.P., Heckman T.M., 1989a, ApJ, 341, 658
- Smith E.P., Heckman T.M., 1989b, ApJS, 69, 365
- Snios B., Nulsen P.E.J., Wise M.W., et al. 2018, ApJ, 855:71
- Wilson A.S., Smith D.A., Young A.J., 2006, ApJ, 644, L9
- Yaji Y., Tashiro M.S., Isobe N., et al., 2010, ApJ, 714, 37